Rakenteiden Mekaniikka (Journal of Structural Mechanics)
Vol. 58, No. 2, 2025, pp. 86–109
http://rakenteidenmekaniikka.journal.fi
https://doi.org/10.23998/rm.148552
© 2025 The Authors
Open access under the license CC BY 4.0

VERTAISARVIOITU
KOLLEGIALT GRANSKAD
PEER-REVIEWED
www.tsv.fi/tunnus

Indentation hardness of 3D-printed metals

Gia Khanh Pham[1], Ruth Domes, Ümit Mavis, Johannes Ernstberger, Christian Seidel, Constanze Eulenkamp, Christine Hausner-Henzel, Anh Son Nguyen and Gia Vu Pham

Summary Additive manufacturing is typically used for rapid prototyping and the production of small to medium quantities of complex parts. The quality of 3D-printed metallic parts depends on the printing process parameters and material behaviour. In order to characterize the mechanical properties of materials, the nearly non-destructive micro-indentation hardness testing of additively manufactured steel and aluminium alloy using Laser Powder Bed Fusion technology was investigated in this study. The micro-hardness and modulus of elasticity of hot work tool steel AISI H13 (1.2344) were evaluated to study the influence of printing parameters, such as laser power and laser scanning speed. While no pile-up or sink-in effects were detected in the steel samples, the pile-up effect was observed during the hardness measurement of the aluminum alloy AlMg1Si AA-6061. Since the pile-up effect leads to an overestimation of the measured hardness, a correction factor was applied to account for this deviation, resulting in an adjusted value approximately 7% lower than the initially measured hardness for the aluminum alloy. In addition, the statistical reliability of the measured hardness properties of the 3D-printed metals was evaluated using the Weibull distribution. It was demonstrated that the indentation test is highly suitable for analyzing small additively manufactured samples with relatively little effort while delivering high statistical reliability and providing meaningful insights into the mechanical properties of the materials, such as micro-hardness and indentation modulus.

Keywords: indentation hardness, pile-up effect, LPBF 3D-printing technology, AISI H13 steel, Al-alloy AlMg1Si AA-6061

Received: 10 October 2024. Accepted: 9 June 2025. Published online: 23 June 2025.

Introduction

Additive manufacturing of metals is widely used across various industries, enabling the rapid development of prototypes and the production of components with highly complex geometries using both existing and new materials or combinations thereof [1]. In particular, the quality of 3D-printed metallic components depends on numerous influencing factors, including printing process parameters and material behavior. To

[1]Corresponding author: gia-khanh.pham@hm.edu

optimize the 3D printing process, understanding material behaviors and changes in material properties is crucial. For instance, 3D-printed metallic components using Laser Powder Bed Fusion (LPBF) can exhibit various special features and defects such as texture, residual pores, unmelted or inconsistently melted areas, and the formation of heat-affected zones, as well as a finer grain structure due to very rapid localized heating and cooling [2]. Consequently, post-processing heat treatment is often necessary for these metallic components to improve and optimize the material properties.

In addition to microstructure, the mechanical properties of 3D-printed materials are of great importance and need to be analysed. Instrumented indentation hardness testing provides a rapid and nearly non-destructive method for characterizing the mechanical properties of materials [3]. Although this technique is not new and has been employed for many years, it is now widely applied to a broad spectrum of materials, ranging from powders and bulk materials to thin films. For instance, indentation hardness and elastic modulus have been investigated in powders such as 316L stainless steel for additive manufacturing [4], as well as in metals like aluminum [5], steel [6], WC–12Co hardmetals [7], titanium and its alloys [8, 9], ceramics and glasses [10, 11], and particularly in thin films and protective coatings [12, 13]. Micro- and nanoindentation are particularly useful for analyzing heterogeneous microstructures, phase distributions, and local variations in mechanical properties, especially in cases where only small material volumes are available for testing.

Due to the rapid advancement of additive manufacturing technologies in recent years, there has been growing interest in understanding the complex relationship between these processes and the resulting material characteristics. F. Khodabakhshi et al. employed nanoindentation testing to investigate the influence of processing cooling rates on the phase structure and the resulting nanoscale deformation mechanisms in functionally graded 316L austenitic and 410L martensitic stainless steels fabricated via Directed Energy Deposition (DED) [14]. This approach provides valuable insights into the variation of grain morphologies, geometries, and orientations across different layers, which are influenced by changes in processing parameters.

The microstructural characteristics and mechanical properties of metals produced by various 3D printing processes have also been extensively studied. For instance, stainless steel 316L fabricated via Laser Powder Bed Fusion (LPBF) has been investigated for its structural and mechanical behavior [15]. Another study [16] utilized nanoindentation testing to examine the influence of volumetric energy density (VED) and the effects of post-heat-treatment nitriding on the creep behavior of H13 hot work tool steel produced by Selective Laser Melting (SLM). Similarly, Inconel 718 alloy manufactured using Laser Powder Bed Fusion was analyzed to assess its microstructural evolution and mechanical properties in comparison to its cast and forged counterparts [17]. Key process parameters such as laser power, scan speed, and spot size, along with their resulting volumetric energy density, were systematically varied to assess their influence on the mechanical performance and overall quality of additively manufactured Inconel 718 components [18].

Furthermore, the influence of process interruptions on the microstructure and mechanical properties of titanium components produced via Wire Arc Additive Manufacturing (WAAM) was investigated in [19]. The study revealed that such

interruptions disrupt the thermal dynamics responsible for interlayer bonding, resulting in significant defects such as porosity and cracking, which ultimately degrade the mechanical performance of the printed parts. In a related study, C. Schneider-Maunoury et al. examined the mechanical properties of a Ti-xNb functionally graded material (FGM) fabricated using the CLAD® additive manufacturing process [20]. The findings demonstrated the effectiveness of indentation testing not only for determining hardness, but also for extracting additional mechanical parameters such as Young's modulus, yield strength, and the work-hardening exponent in heterogeneous materials.

The objective of this study is to investigate the micro-indentation hardness of additively manufactured metals, specifically hot work tool steel AISI H13 (1.2344) and aluminum alloy AlMg1Si AA-6061 produced via Laser Powder Bed Fusion (LPBF), in order to understand the influence of printing process parameters on the mechanical properties of these materials. In addition, the study aims to explore the capabilities and limitations of the micro-indentation testing method for characterizing the mechanical behavior of 3D-printed metallic components.

Theoretical background

Micro- and nano-indentation test

For the determination of hardness and other material parameters the instrumented indentation test can be applied for the following three ranges [21]:

- Macro range: $2\ N \leq$ Indentation Force (F) ≤ 30 kN
- Micro range: Indentation Force (F) < 2 N; Indentation Depth (h) > 0.2 µm
- Nano range: Indentation Depth (h) ≤ 0.2 µm.

With minimal forces, such as in hardness testing in the micro range and especially in the nano range, the indentation becomes smaller and reaches the resolution limit of the optical microscope. Therefore, the area of the indentation cannot be directly determined [22]. This problem can be addressed using an instrumented indentation test, where an indenter (pyramid-shaped Vickers or Berkovich) penetrates the specimen at a specified load rate until the maximum force is achieved (Fig. 1). This is followed by unloading until the force and the penetration depth return to zero.

During the loading and unloading cycle, the load and penetration are continuously recorded using high-resolution instruments (Fig. 2) [3]. From the load-penetration data obtained, the hardness and modulus of elasticity can be determined using a method developed by Oliver and Pharr in 1992 [24].

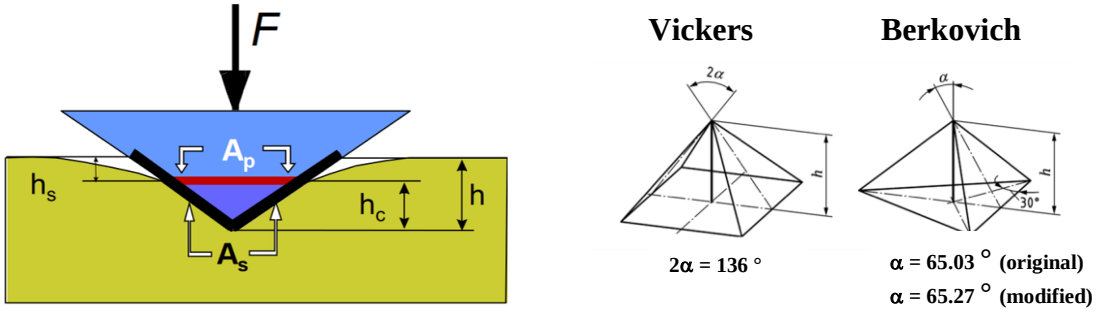

Figure 1. a (left): Indentation hardness test [23] (h: indentation depth, h_c: contact depth, h_s: elastic depth, A_s: surface area, A_p: projected contact area); b (right): Pyramid-shaped Vickers and Berkovich indenter [21].

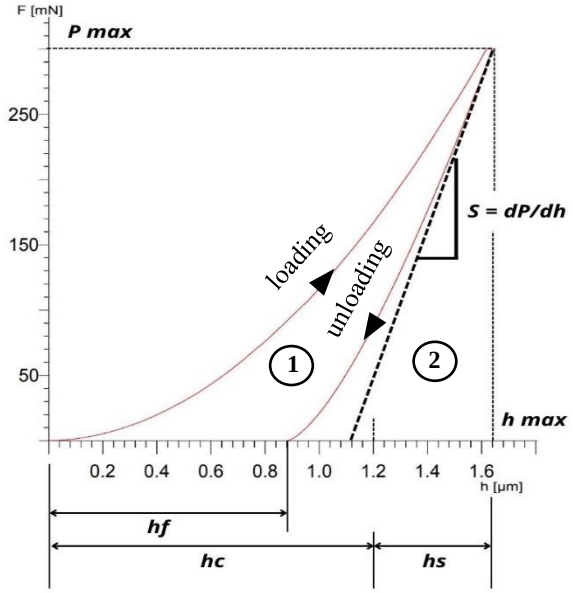

Figure 2. Load-Penetration depth curve with stiffness S, maximum load P_{max}, maximum depth h_{max}, contact depth h_c, elastic recovery h_s and the final depth h_f (Source: Adapted from [21], [24]).

In the Oliver and Pharr method, the elastic recovery h_s and the contact depth h_c are determined using the following formula:

$$h_s = \varepsilon \frac{P_{max}}{S} \tag{1}$$

$$h_c = h_{max} - h_s = h_{max} - \varepsilon \frac{P_{max}}{S} \tag{2}$$

where

- h_{max} is the maximum indentation depth.
- P_{max} is the maximum applied load.

- S is the stiffness of the contact, which is the slope of the unloading curve at P_{max}.
- ε is a geometric constant that depends on the indenter shape (for a Berkovich indenter, $\varepsilon \approx 0.75$).

The projected contact area A_p is defined as the cross-sectional area of contact between the indenter and the sample at the maximum load P_{max}. It is calculated using the contact depth h_c and the geometry of the indenter. For a perfect Berkovich indenter, the projected contact area A_p is given by:

$$A_p(h_c) = 24.5h_c^2 \quad (3)$$

The most frequently used indenters for indentation testing have a pyramid-shaped geometry (Fig. 1b). The Vickers indenter is used in nano-hardness testing as well as in micro- and macro-hardness testing. Its base is square, and the angle between two opposite faces of the pyramid is 136°. However, the Berkovich indenter is typically used in micro- or nano-hardness testing. The three-sided pyramid tip of the Berkovich indenter has the advantage of being easier to fabricate with precise control, ensuring more accurate indentation meassurements, whereas the four-sided Vickers pyramid requires more effort in the grinding process, making sharp geometries difficult to achieve [22, 25]. The dihedral angle of the original Berkovich indenter is 65.03°, as this geometry maintains the same surface area A_s as a Vickers indenter at any given indentation depth. However, most of the Berkovich intenders used have a modified geometry with a dihedral angle of 65.27°, maintaining the same projected area A_p as a Vickers indenter at any given indentation depth [21]. The modified Berkovich indenter with improved tip sharpness and self-similar geometry provide higher accuracy and resolution for shallow indentation depths. It is well suited for nanoindentation, thin film testing, and studying size effects or elastic-plastic transitions at very small scales [26].

In the instrumented indentation test, there are different types of hardness (e.g., Martens or Universal Hardness HM, Indentation Hardness H_{IT}) and material properties (e.g., Indentation Modulus E_{IT}), as well as methods to determine them, depending on the area of the indentation being considered. According to the method of Oliver and Pharr [24] the hardness H in general is defined as the force F (or load P) per contact area A_s or projected contact area A_p of the indentation, considering the dependence of the area as a function of the indentation depth:

$$HM = \frac{F}{A_s(h)} \quad or \quad H_{IT} = \frac{F}{A_p(h_c)} \quad (4)$$

Table 1 gives an overview of a few important parameters determined using the indentation test. According to the standard DIN EN ISO 14577-1:2015-1, the parameters can be defined as follows [21]:

- The Martens hardness, HM, is calculated from the values of the force-penetration depth curve during the application of the test force, preferably after the specified test force has been reached. The Martens hardness contains the plastic and elastic deformation and therefore this hardness value can be calculated for all materials.
- The Martens hardness can also be determined from the slope m_s of the rising force-indentation depth curve, so called HM_s. The method for determining the Martens hardness HM_s from the slope of the rising force-penetration depth curve has the

advantage of being independent of the uncertainty of the zero-point determination and the specimen roughness.

- The indentation hardness H_{IT} is a measure of the resistance to permanent deformation or damage and is commonly described or used in numerous studies in the context of nano-indentation.
- The indentation modulus E_{IT} is determined from the tangent of the force reduction-indentation curve at the point F_{max}. The indentation modulus E_{IT} is comparable to the modulus of elasticity. Deviations from the modulus of elasticity of the sample material are the result of pile-up and sink-in effects during the indentation process.
- The Vickers hardness HV cannot be directly assessed, because the surface area can only be measured indirectly when determining nano hardness. However, in order to compare the hardness of materials, the indentation hardness H_{IT} can be converted into Vickers hardness HV under certain conditions. Because the projected contact area A_p, as used by Oliver and Pharr, differs by about 7% from the actual contact area A_s used in Vickers hardness measurements, the calculated Vickers hardness value is approximately 7% lower than the corresponding indentation hardness [22]. Although H_{IT} can be correlated with HV in this way, an HV value calculated in this manner should not be used as a substitute for a directly measured HV value.

There are further measurement results depending on the measurement methods, which are not detailed here, such as creep indentation C_{IT} and indentation relaxation R_{IT}. Another parameter is η_{IT}, which describes the ratio between the plastic deformation work W_{plast} (area between the loading and unloading segment of the force-indentation depth curve, (1) in Fig. 2) and the work of elastic deformation W_{elast} (area under the unloading segment of the force-indentation depth curve, (2) in Fig. 2).

Factors affecting micro- and nano-indentation results

Instrumented indentation test results are influenced by various factors, including indenter geometry, surface defects (such as roughness, scratches, and pores), indentation size, as well as pile-up and sink-in effects [22]. A smooth and clean surface of the material is necessary. Otherwise, the indentation depth and the actual contact area of the indenter depend on its position, resulting in varying hardness measurements. Figure 3 illustrates the measurements taken on both smooth and rough sample surfaces. To ensure that the measurement error of the indentation depth h remains below 5%, a surface roughness Ra is required such that $h > 20 \times Ra$ [21].

Table 1. Measured parameters of the micro- and nano-indentation test [21]

Parameter	Description	Vickers	Berkovich (original)
Martens (Universal) Hardness HM	$HM = \frac{F}{A_s(h)}$ (5)	$A_s(h) = 26.43 \times h^2$ (6)	$A_s(h) = 26.43 \times h^2$ (7)
Martens Hardness HM_s	$HM_s = \frac{1}{m_s^2 \times A_s(h)/h^2}$ (8)	$A_s(h) = 26.43 \times h^2$	$A_s(h) = 26.43 \times h^2$
Indentation Hardness H_{IT}	$H_{IT} = \frac{F_{max}}{A_p(h_c)}$ (9)	$A_p(h_c) = 24.5 \times hc^2$ (10)	$A_p(h_c) = 23.97 \times hc^2$ (11)
Indentation Modulus E_{IT}	$E_{IT} = \frac{1-(\nu_s)^2}{\frac{1}{E_{r,n}} - \frac{1-(\nu_i)^2}{E_i}}$ (12)	with ν_s: Poisson's ratio of the sample ν_i: Poisson's ratio of the indenter E_r: reduced module for indentation contact E_i: modulus of the indenter	
Vickers hardness HV	• No direct determination with nanoindentation • H_{IT} can be converted to HV under certain condition.	$HV = 94.53 \times H_{IT}$ (13)	$HV = 92.44 \times H_{IT}$ (14)

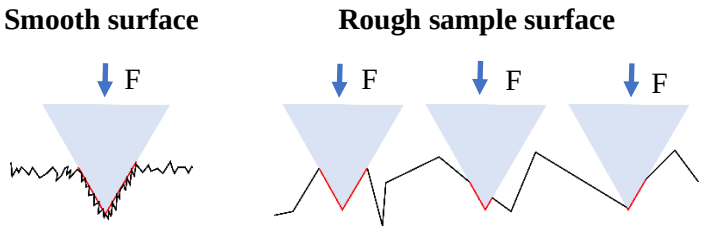

Figure 3. Smooth surface on the left. On the right side the roughness causes position-dependent hardness measurement (adapted from [22]).

Pores within the sample can significantly affect the accuracy of indentation hardness measurements, as these tests probe only very small material volumes. Wei Li et al. [27] used nanoindentation to investigate the influence of pores in additively manufactured metals produced by Directed Energy Deposition (DED) and found that pore sizes ranged from a few microns to several hundred microns. Most pores were micro-pores smaller than 50 µm, although medium-sized (50–100 µm) and large pores (> 100 µm) were also present. Similarly, the occurrence of large pores-measuring several hundred micrometers-

has been reported in parts produced using other additive manufacturing techniques, such as Laser Powder Bed Fusion (LPBF). Even under low-energy laser processing conditions, average pore radii between 22 and 29 μm have been observed [28]. In contrast, the projected contact area in micro- and nanoindentation ranges from a few to several hundred square micrometers (corresponding to indentation side lengths of a few to several tens of micrometers), depending on the applied load, making it highly susceptible to the influence of pores. These pores reduce the local load-bearing capacity due to both a diminished contact area and stress concentrations at the pore edges, leading to an underestimation of the material's true hardness [27]. As the distance from a pore increases, both the elastic modulus and hardness tend to rise. Furthermore, hardness values measured near smaller pores are generally higher than those near larger pores. Consequently, the presence of pores can cause the Oliver–Pharr method to yield artificially low hardness values, increase data scatter, and reduce the overall reliability of nano- and micro-hardness measurements.

Pile-up and sink-in effects also influence the indentation [22, 29, 30]. While the indentation process causes plastic deformation, pile-up and sink-in effects can occur due to work-hardening mechanisms (Fig. 4). In this case, the material is either piled up at the edge of the contact (pile-up) or sinks in (sink-in). These effects lead to changes in the size of the contact area, which result in changes in the hardness parameters measured. Pile-up means that a smaller projected area A_p is calculated than the actual or true contact area (underestimation of the true contact area), leading to higher hardness and modulus of elasticity values determined by the Oliver and Pharr method than the true values (overestimation of hardness). Similarly, the sink-in effect causes an overestimation of the true contact area and an underestimation of hardness. Therefore, when pile-up or sink-in occurs, the measured hardness and modulus of elasticity need to be corrected to a lower value (for pile-up) or a higher value (for sink-in). Materials with low work-hardening capacity (e.g., strain-hardened metals and metallic glasses) tend to exhibit more pronounced pile-up, whereas materials with a high work-hardening rate (e.g., well-annealed soft metals like copper) are more likely to sink in [29].

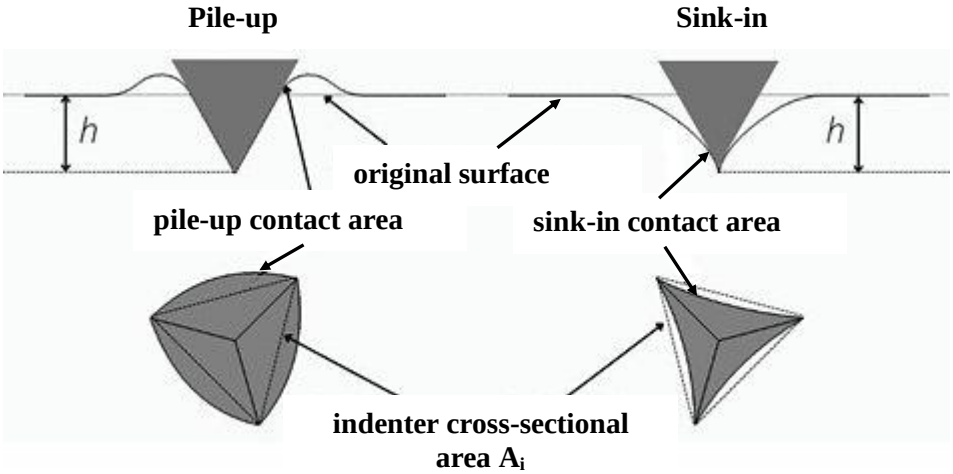

Figure 4. Pile-up on the left side, hardness is overestimated. Sink-in on the right side, hardness is underestimated (Source: Adapted from [29]).

McElhaney et al. [29] developed a method to correct the pile-up and sink-in effects. This correction needs to be performed for each newly examined material. Since the projected area A_p calculated is underestimated by the pile-up effect and overestimated by the sink-in effect, the cross-sectional area of the indenter A_i is additionally considered in the correction. This can be determined from Scanning Electron Microscope (SEM) images. The correction factor α is calculated according to Equation (15) and describes the ratio of the actual or true indentation projected contact area A_c to the cross-sectional area of the indenter A_i. In SEM images, A_i is determined as the area of the triangle marked by the corners of the indentation. The pile-up effect occurs when $\alpha > 1$, meaning the contact area is greater than the cross-sectional area of the indenter. Conversely, the sink-in effect occurs when $\alpha < 1$, indicating that the contact area is smaller than the indenter's cross-sectional area.

$$\alpha = \frac{A_c}{A_i} \tag{15}$$

The correction factor is used to calculate the corrected hardness in Equation (4). The indentation hardness is corrected as follow:

$$HM = \frac{F}{aA_s(h)} \quad or \quad H_{IT} = \frac{F}{aA_i} \tag{16}$$

Materials and methods

3D-printed materials and sample preparation

In this study, two additively manufactured metals – hot work tool steel AISI H13 (1.2344) and aluminum alloy AlMg1Si AA-6061 – were chosen for the micro-indentation tests. All samples were 3D-printed using the Laser Powder Bed Fusion (LPBF) technology with the following parameters (Table 2):

Table 2. LPBF printing parameters of steel and Al-alloy samples.

3D-Printing parameters	AISI H13 hot work tool steel	Al-alloy AlMg1Si AA-6061
LPBF system	Alpha Laser AL-METAL 250	GE Concept Laser M2 - Series 5
Powder layer thickness	30 µm	50 µm
Hatching distance	49 µm	120 µm
Laser power	136 W (standard) or 102 W (25 % lower)	350 W
Laser wavelength	1070 nm	1070 nm
Laser focus diameter	50 µm	180 µm
Laser scan speed	1.133 m/s (standard) or 1.586 m/s (40 % higher)	1.500 m/s

For micro-indentation tests, small samples were cut from 3D-printed metals to prepare the cross-sections. Cross-sections are then ground and polished. Initially, the samples

were ground with sandpaper (200-2000 grit) to remove coarse surface irregularities. For smoother surfaces, subsequent polishing was performed using diamond paste or suspension. The gradation of the diamond grit used for polishing was 6 µm, 3 µm, and 1 µm. The results of grinding and polishing were examined using an optical microscope. By grinding and polishing the samples, the pores contained in the material became visible. To remove water and diamond residues from these pores, all samples were cleaned in an ultrasonic bath.

The aluminum alloy is very soft compared to AISI H13 steel. Diamond residues from previous polishing steps accumulated in the pores and caused scratches on the surface during subsequent steps. Therefore, ultrasonic bath cleaning was performed after each polishing step during the preparation of this sample. Despite the cleaning, not all diamond particles could be removed, making scratches on the surface unavoidable. These areas were particularly susceptible to errors during indentation measurements.

Hardness measurement

The micro- and nano-hardness measurements were conducted using the Picodentor HM500 from Helmut-Fischer GmbH (Sindelfingen, Germany). The device consists of a measuring head with the indenter, sample holder, microscope (with magnifications of 5x, 20x, and 50x), and a programmable X-Y stage (Fig. 5). Generally, the indenter impacts the sample at a velocity of $v < 0.1$ µm/s. With a resolution of ≤100 nN, a test force ranging from 0.005 mN to 500 mN can be applied. The maximum indentation depth is 150 µm with a resolution of ≤ 40 pm.

The hardness of each sample was determined multiple times at different positions using array measurement mode to obtain good statistical results. Arrays of 30 measuring points each, with precise positions, were programmed into the measurement software for position-dependent measurement. Several arrays could be chosen for a measurement. The total number of measuring points varied depending on the sample size and surface properties, ranging from 120 to 210 points. The samples were measured vertically and horizontally. Vertically means that the indenter penetrated between the 3D-printed layers (build direction or Z printing direction), whereas in the horizontal samples, the force was applied perpendicular to the printed layer (build layer or X-Y printing direction). The measured samples are listed in Table 3. The steel and aluminum reference samples (samples no. 5, 6, and 7) were 3D-printed using an *optimized standard program* with the parameters specified in Table 2. For these reference samples, the printing parameters were fine-tuned to achieve the highest possible quality, characterized by minimal porosity and favorable melting behavior of the particles. This optimization was carried out in previous laboratory studies. In the case of the steel samples, the 3D printing parameters were additionally varied to investigate their influence on the indentation hardness.

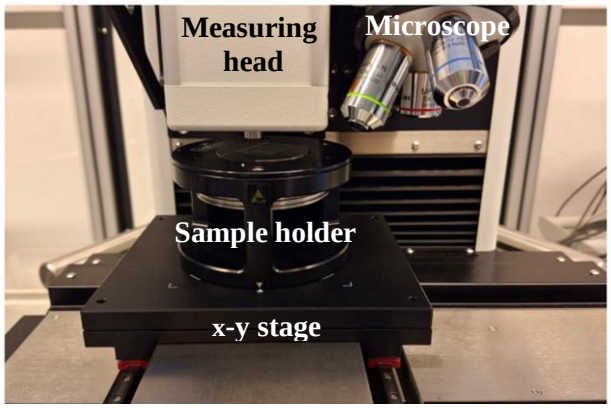

Figure 5. Picodentor HM500 with measuring head, microscope, sample holder and x-y stage.

Table 3. List of measured samples.

No.	Samples	Description
1	ST1-XY	3D-printed steel with 40 % higher laser scan speed, X-Y printing direction (build layer)
2	ST1-Z	3D-printed steel with 40 % higher laser scan speed, Z printing direction (build direction)
3	ST2-XY	3D-printed steel with 25 % lower laser power, X-Y printing direction (build layer)
4	ST2-Z	3D-printed steel with 25 % lower laser power, Z printing direction (build direction)
5	ST0-XY	3D-printed steel with optimized standard program, X-Y printing direction (build layer)
6	ST0-Z	3D-printed steel with optimized standard program, Z printing direction (build direction)
7	AL0-XY	3D-printed AlMg1Si alloy with optimized standard program, X-Y printing direction (build layer)

In this study, the micro-indentation measurements were performed using an original Berkovich indenter. The test parameters used in this study are listed as follows: Test force F_{max} of 300 mN, loading/unloading time of 20 s, and a holding time at F_{max} of 5 s. The following parameters were determined as results: Martens or Universal hardness HM, Martens hardness HM_s from the slope of the rising force-penetration depth curve, Indentation hardness H_{IT}, Indentation modulus E_{IT}, Vickers hardness HV, projected contact area A_p of the indenter, distance h_c from the tip, and maximum penetration depth h_{max} with maximum test force. Additionally, the pile-up and sink-in effects were checked

during the indentation tests. If these effects occur, the correction factor α is determined and the hardness is accordingly corrected.

The Weibull distribution is used to analyze the measured Martens hardness. Like strength testing, this distribution is employed to determine errors or failure criteria. The evaluation of hardness values using the Weibull distribution aims to capture statistical variations in the measurement data. Defects, such as pores and inhomogeneities in the material, lead to a scattering of the hardness values, which can be well described by the Weibull distribution [31]. The Weibull function is utilized for ceramics [32], metals such as steels [33, 34], Ti-alloys [35], Al-alloys [36], and metallic glasses [37].

A program is written in Matlab to evaluate the Weibull function for the calculations, utilizing MATLAB's ”Statistics and Machine Learning Toolbox”. Since hardness measurement is a surface measurement, there are two ways to interpret the results. In one option, all data points, including incorrect measurements, are considered, whereas, in the other option, outliers are excluded.

The Weibull distribution is defined in such a way that the probability of failure P_f increases with the increasing variable x [31]. x is the measured Martens hardness in this study.

$$P_f = 1 - e^{-\left(\frac{x-x_u}{x_0}\right)^m} \tag{17}$$

The parameter x_u corresponds to the threshold below which the sample does not fail. The scale parameter x_0 is a measure of the scale of the distribution or the characteristic life. A larger x_0 value widens the distribution, while a smaller x_0 value narrows it. In reliability engineering and life data analysis the characteristic life x_0 is defined as the age at which 63.2% of the units will have failed. That means 63.2% of the values in the distribution are less than the scale parameter [38]. The shape of the distribution function is determined by the parameter m, also known as the Weibull modulus. The Weibull modulus m is a measure of the variation width. For analysis using the Weibull distribution, equation (17) is often presented in a double logarithmic form:

$$\ln\left[ln\left(\frac{1}{1-P_f}\right)\right] = mlnx - mlnx_0 \tag{18}$$

By applying linear regression to the data in the double logarithmic coordinate system, the slope of the fitting line can be determined, representing the Weibull modulus. A high modulus m or a high slope indicates a narrow distribution function. For the tested samples, this implies that failure due to hardness variations is less likely to occur.

Results and discussion

Micro-indentation hardness of AISI H13 steel and AlMg1Si alloy AA-6061

The results of the hardness measurements indicate that some indentation tests failed, as no values for the projected area A_p and the penetration depth h_c could be calculated. In some other cases, the measured hardness values show significant deviations. Strongly deviating hardness values or outliers are defined as measurement points that lie outside

the measurement tolerance. Accordingly, a value is considered an outlier if it is more than 1.5 times the interquartile range IQR above the upper quartile Q3 or below the lower quartile Q1. The first quartile Q1 is the value below which 25% of the data points fall, and the third quartile Q3 is the value below which 75% of the data points fall. Thus, lower outliers are those below Q1−1.5×IQR and upper outliers are those above Q3+1.5×IQR. The IQR, or interquartile range, indicates the spread of the middle 50% of the data (IQR = Q3 - Q1). [39]

To determine the cause of the measurement errors, the indentations were examined under an optical microscope. The microscopic images revealed that the indentations were either partially or completely located in a pore of the material (Fig. 6a). The indentations corresponding to the measured values identified as outliers are significantly more recognizable. The most common feature of the microscope images with these measured values are surface irregularities such as scratches or polishing marks (Fig. 6b).

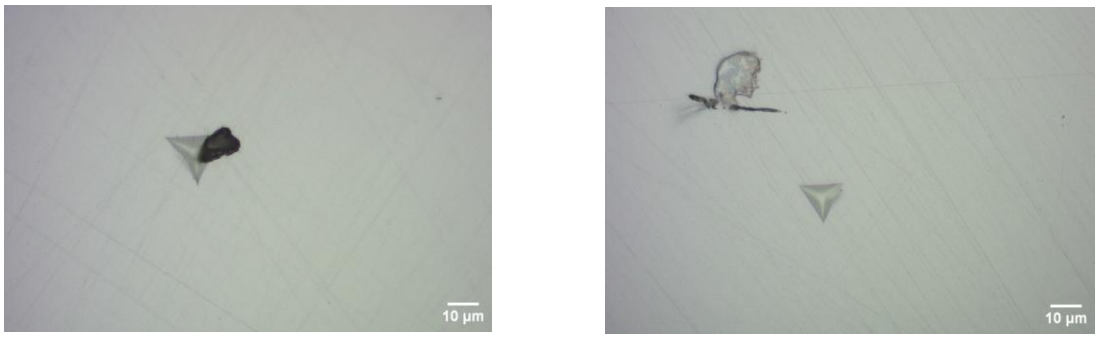

Figure 6. a (left): Failed measurement caused by a pore in the steel sample; measurement without calculating the projected area A_p and the penetration depth h_c. b (right): Incorrect measured value due to outliers in a steel sample: Calculated indentation hardness is outside the tolerance due to surface irregularities.

The results in Table 4 show that the 3D-printed AISI H13 steel samples produced with an optimized standard program have clearly the lowest number of errors. When the samples are printed at 40% higher laser scanning speed, more measurement errors occur. There are more errors without measured values in the build layer or X-Y printing direction compared to the build direction or Z printing direction. Particularly, samples printed with 25% lower laser power exhibit the highest number of measurement errors without measured values, reaching 10%. This indicates that these samples should have significantly more defects and higher porosity in the X-Y printing direction than in the Z printing direction, leading to a higher number of measurement errors without measured values. In comparison, the number of errors outside the tolerance (outliers) varies between approximately 1% to 3%.

Likewise, the 3D-printed AlMg1Si alloy samples show a low level of errors. There are no errors without measured values, and 1.7% errors outside the tolerance (outliers). This indicates a good quality of the printed AlMg1Si alloy samples.

The results above are consistent with the observed microscope images. AISI H13 steel samples produced with lower laser power and higher laser scanning speed exhibit high

porosity, including large pores. In contrast, steel samples printed with an optimized standard program and AlMg1Si alloy samples show significantly lower porosity. The quality of steel samples in the X-Y printing direction is much better than in the Z printing direction.

Table 4. Measurement errors of the individual samples are divided into errors without measured values and errors outside the tolerance (outliers).

No.	Samples	Number of measurement points	Errors without measured values [%]	Errors outside the tolerance [%]
1	ST1-XY	210	5.7	1.0
2	ST1-Z	180	2.2	2.8
3	ST2-XY	210	10.0	2.9
4	ST2-Z	180	1.1	2.8
5	ST0-XY	120	0.0	2.5
6	ST0-Z	120	0.0	0.8
7	AL0-XY	120	0.0	1.7

After eliminating all measurement errors, the measured values are statistically analyzed. The mean values of hardness, modulus of elasticity, and their standard deviations are summarized in Table 5.

The results in Table 5 confirm the previous observations about the measurement errors reported in Table 4. Although all AISI H13 steel samples exhibit similar mean values for hardness (HM ~ 4800 MPa) and indentation modulus (E_{IT} ~ 230 GPa), the standard deviations show significant differences depending on the 3D printing parameters. All samples exhibit higher standard deviations in the X-Y printing direction compared to the Z printing direction. 3D-printed steel samples fabricated with an optimized standard program show the lowest standard deviation, ranging between 2% and 7%. However, the standard deviation increases significantly with higher laser scanning speeds and lower laser power. Samples printed with 25% lower laser power exhibit the highest standard deviation, around 10%, the cause of which can be traced back to the higher number of small material defects and pores. As expected, the AlMg1Si alloy samples show significantly lower hardness values (HM = 894 MPa) and indentation modulus (E_{IT} = 94 GPa) compared to the steel samples. The AlMg1Si alloy samples also exhibit a low standard deviation, ranging from 2% to 4%. It should be noted that potential pile-up or sink-in effects have not yet been considered and corrected in all samples.

Moreover, the steel samples exhibit an average projected contact area A_p of 49 µm², a tip distance h_c of 1.42 µm, and a maximum penetration depth h_{max} of 1.5 µm. The AlMg1Si alloy samples show a larger average projected contact area A_p of 290 µm², a tip distance h_c of 3.5 µm, and a maximum penetration depth h_{max} of 3.6 µm. The standard

deviation varied between 1% and 13%, depending on the material and printing parameters.

Table 5. Mean value and standard deviation of the measured values of AISI H13 steel and AlMg1Si alloy. The standard deviation in % is shown in round brackets.

No.	Samples	HM [MPa]	HM_s [MPa]	H_{IT} [MPa]	HV	E_{IT} [GPa]
1	ST1-XY	4745 ±385 (8.1 %)	5099 ±452 (8.9 %)	6265 ±589 (9.4 %)	580 ±54 (9.3 %)	230 ±15 (6.5 %)
2	ST1-Z	4679 ±267 (5.7 %)	5028 ±307 (6.1 %)	6117 ±411 (6.7 %)	566 ±38 (6.7 %)	236 ±8 (3.4 %)
3	ST2-XY	4737 ±452 (9.5 %)	5090 ±504 (9.9 %)	6322 ±683 (10.8 %)	585 ±63 (10.8 %)	218 ±18 (8.3 %)
4	ST2-Z	4892 ±283 (5.8 %)	5197 ±315 (6.1 %)	6483 ±442 (6.8 %)	600 ±41 (6.8 %)	233 ±10 (4.3 %)
5	ST0-XY	4775 ±196 (4.1 %)	5045 ±231 (4.6 %)	6237 ±233 (3.7 %)	577 ±21 (3.7 %)	237 ±16 (6.7 %)
6	ST0-Z	4832 ±122 (2.5 %)	5107 ±133 (2.6 %)	6295 ±187 (3.0 %)	582 ±17 (2.9 %)	241 ±4 (1.7 %)
7	AL0-XY	894 ±31 (3.5 %)	901 ±34 (3.8 %)	1040 ±38 (3.7 %)	96 ±4 (4.2 %)	94 ±2 (2.1 %)

The Weibull distributions of the measured Martens hardness *HM* of AISI H13 steel and AlMg1Si alloy samples were analyzed using MATLAB's ”Statistics and Machine Learning Toolbox”. The cumulative distribution functions were presented in a double logarithmic plot, where the x-axis represents the measured Martens hardness *HM* and the y-axis represents the cumulative failure probability *F(x)* (Figs. 7a and 7b). *F(x)* at a given Martens hardness value *x* indicates the proportion of messurements that have a hardness less than or equal to that value *x*. To determine the Weibull modulus m, a linear fit of the data was performed. The slope of the regression line corresponds to the Weibull modulus

m. The Weibull modulus m, along with its lower and upper confidence limits and the p-value, are presented in Table 6.

The calculated Weibull modulus m can further confirm the results reported in Tables 4 and 5. The larger the Weibull modulus, the smaller the hardness deviations within a sample. Accordingly, the widest Martens hardness distribution is observed in AISI H13 steel samples printed with 25% lower laser power (ST2) or at 40% higher laser scanning speed (ST1), specifically in the X-Y printing direction (Fig. 7a). This can be seen in the more gradual slope of the regression line, indicating greater variability in the hardness values measured for these two samples. Conversely, the hardness of the AISI H13 steel samples fabricated with an optimized standard program (ST0) exhibits the smallest hardness deviation within the sample. The ST0 samples show a steeper slope of the regression line, resulting in a clearly higher Weibull modulus and more consistent material behavior.

Compared to steel samples fabricated with an optimized standard program, the AlMg1Si alloy samples also exhibit a high Weibull modulus and a steeper slope of the regression line, indicating low variation in the measured hardness values and good material printing quality (Fig. 7b).

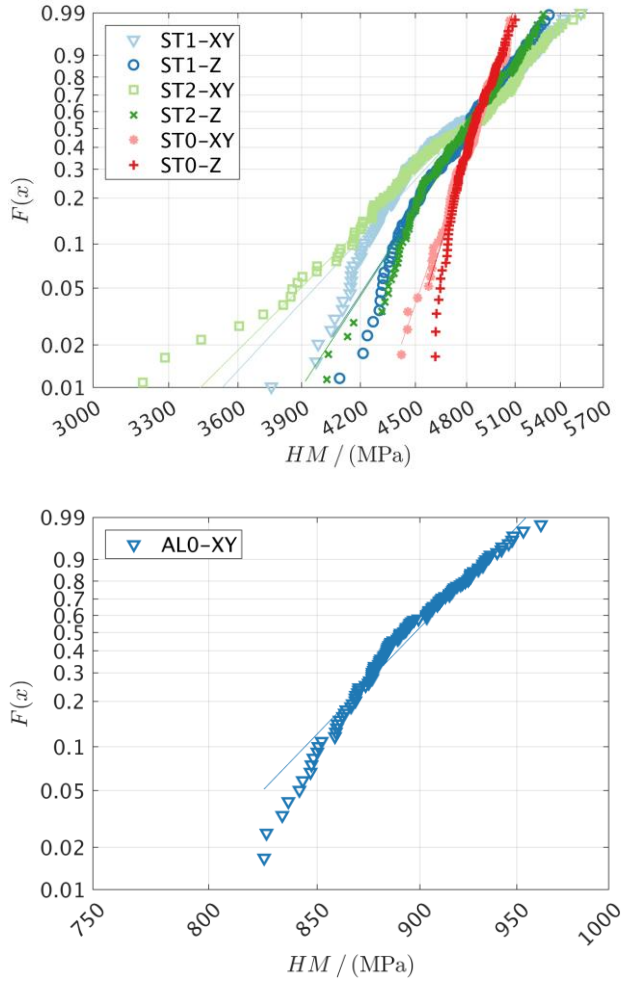

Figure 7. Weibull distribution of samples: AISI H13 steel (top); AlMg1Si alloy (bottom).

The confidence analysis provides the lower and upper limits of the 95% confidence interval for the Weibull modulus (Table 6). With 95% confidence, it can be asserted that the true Weibull modulus falls within the interval defined by the lower and upper confidence limits. For all samples, the confidence intervals are narrow relative to the estimated Weibull modulus m, indicating a high precision in the estimation. The Kolmogorov–Smirnov (KS) test was conducted to assess whether the measured data follow a Weibull distribution [40]. The p-value calculated with this test indicates the agreement of the measured data with the selected Weibull distribution. The null hypothesis – that the data follow a Weibull distribution – is not rejected if the p-value exceeds the significance level of 0.05. If the p-value is greater than 0.05, the data are considered to fit the Weibull distribution well. In general, the higher the p-value, the better the agreement between empirical data and the theoretical distribution. This behavior was consistently observed across all the samples investigated, with p-values ranging from 0.089 to 0.728, thereby indicating a good fit between the calculated Weibull distribution and the measurement data.

Table 6. Weibull module m, lower and upper confidence limits, and p-value of AISI H13 steel and AlMg1Si alloy samples.

No.	Samples	Weibull module m	Lower confidence limit	Upper confidence limit	p-value
1	ST1-XY	14.00	12.57	15.60	0.089
2	ST1-Z	19.82	17.67	22.22	0.670
3	ST2-XY	12.92	11.51	14.51	0.323
4	ST2-Z	20.05	17.87	22.49	0.677
5	ST0-XY	37.64	32.78	43.23	0.728
6	ST0-Z	42.10	36.82	48.14	0.292
7	AL0-XY	30.59	26.76	34.98	0.320

Pile-up effect of AlMg1Si alloy samples

While no pile-up or sink-in effects were observed in the steel samples, the pile-up effect occurred during the hardness measurement of the AlMg1Si alloy, regardless of the amount of applied force. For example, Fig. 8a shows an indentation, which was measured with a reduced force of 5 mN and a loading/unloading time of 10 s without holding time. Figure 8b shows an indentation measured with the standard measurement program used in this study (with a force of 300 mN, a loading/unloading time of 20 s, and a holding time of 5 s). Both indentations were subsequently investigated using a high-resolution Scanning Electron Microscope (SEM), the TESCAN LYRA3 GMU, as the optical microscope of the indentation device Picodentor HM500 was not able to resolve them

accurately, particularly due to the small size of the indentations resulting from the application of minimal force. It can be observed that there is a pile-up of material on the sides of the triangles, independent of the applied load. These pile-ups increase the actual projected area A_p, leading to a lower true hardness value than that calculated using the Oliver and Pharr method. This discrepancy results from an underestimation of the actual contact area, which consequently leads to an overestimation of hardness, as outlined in the section “Factors affecting micro- and nano-indentation results”.

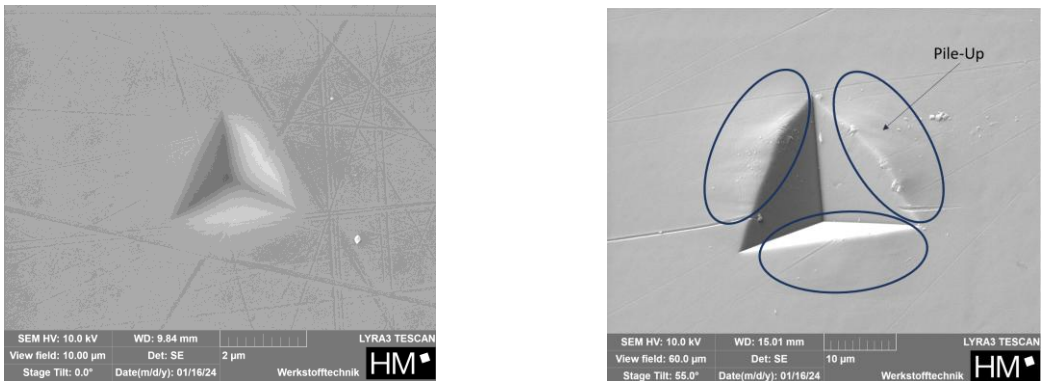

Figure 8. a (left): SEM image of the with a force of 5 mN and loading/unloading time of 10 s without holding time; b (right): SEM image of the with a force of 300 mN, a loading/unloading time of 20 s, and a holding time of 5 s.

The correction factor α is calculated according to equation (15) to determine the magnitude of the error caused by the pile-up effect. Since indentations can be evaluated with sufficient accuracy and less effort using an optical microscope at higher applied loads, the pile-up effect at a standard load of 300 mN was analyzed using a Leica DMR optical microscope. Due to the reduced sharpness of indentation edges in optical microscope images relative to SEM images, ten correction factors were derived from ten optical images per sample and averaged to obtain a representative mean value. Figure 9a presents an optical image of the indentation as an example, clearly showing the pile-up effect. In Figure 9b, the image contrast has been adjusted to provide a clearer visualization of the indentation. This enhanced image was used to determine the cross-sectional area A_i of the indenter and the actual projected contact area A_c, including the pile-up at the edges. Using ImageJ software, these areas were calculated. The cross-sectional area A_i was obtained by tracing the triangular indentation in the optical microscope image (indicated by red lines) and calculating its area. The correction factor α was then calculated as the ratio of the measured projected area A_c to the cross-sectional area A_i.

The results show that the pile-up effect causes a deviation in the area of the AlMg1Si alloy samples of (7.1 ± 3.2) %, with a correction factor α of (1.07 ± 0.03). This means that the hardness values given in Table 5 (without considering the pile-up effect) must be corrected by 7%. Accordingly, the Martens hardness of the AlMg1Si alloy samples should be corrected to a lower value of 835 MPa, instead of the initially measured 894 MPa.

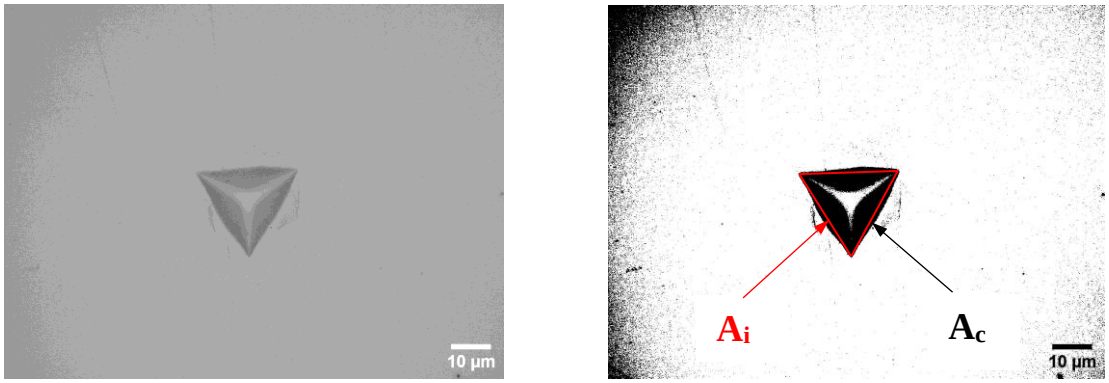

Figure 9. a (left): Optical image of an indentation showing the pile-up effect at an applied force of 300 mN; b (right): Enhanced image with adjusted contrast of the same indentation, used to determine the cross-sectional area A_i of the indenter and the actual projected contact area A_c.

Limitations of the micro-indentation testing method

As discussed, the results of micro-indentation measurements are influenced by a variety of factors, particularly the material's heterogeneity, including defects and phase formation. Not all microstructural components can be effectively analyzed using this method. In this study, the steel samples exhibited a maximum penetration depth h_{max} of 1.5 µm and an average projected contact area A_p of 49 µm² under an applied load of 300 mN. This corresponds to an equivalent circular diameter of approximately 7.9 µm for the same projected area. In comparison, the AlMg1Si alloy samples showed a maximum penetration depth of 3.6 µm and a larger average projected contact area of 290 µm², corresponding to an equivalent diameter of approximately 19.2 µm. This implies that defects or phases within, or exceeding, the size range of approximately 8–20 µm can significantly influence the measurement results. For instance, in samples produced with a 40% higher laser scanning speed and a 25% reduction in laser power, numerous large pores (>100 µm) were observed, which can lead to inaccurate or failed measurements. Defects and pores of similar or smaller dimensions also contribute to increased variability in the measured values and are generally associated with lower measured hardness.

Other microstructural features significantly smaller than 8 µm – such as grain boundaries, precipitates, or fine phases – cannot be reliably characterized using micro-indentation at this load level. Considering the measured maximum penetration depths of 1.5–3.5 µm for the steel and aluminum alloy samples, thin films of comparable thickness and material cannot be accurately characterized using micro-indentation, as the influence of the substrate would dominate the measurement. For such thin films and microstructural features, lower indentation forces (i.e., nanoindentation) combined with optimized testing parameters (e.g., loading rate and holding time) are required. Moreover, the optical microscope built into the Picodentor HM500 indentation device used in this study, with a maximum magnification of 50x, does not permit precise targeting of very small-scale microstructural features.

Conclusions and outlook

In this study, the hardness of 3D-printed AISI H13 steel and AlMg1Si alloy AA-6061 was investigated using the micro-indentation test. It was demonstrated that this nearly non-destructive measurement method is highly suitable for analyzing small additively manufactured samples with relatively little effort while delivering high statistical reliability and providing meaningful insights into the mechanical properties of the materials, such as micro-hardness and indentation modulus. The statistical reliability of the measured properties can be captured very well with the Weibull distribution, correlating with the microstructural properties of the analyzed materials. Microstructural defects, such as pores and surface irregularities, lead to measurement errors, which were addressed in this work using a developed evaluation method.

The analyzed AISI H13 steel samples, produced with varying 3D printing parameters, were measured in different orientations (X-Y and Z printing directions). While all AISI H13 steel samples display similar mean values for hardness and indentation modulus, their standard deviations and Weibull moduli vary significantly depending on the 3D printing parameters. Samples produced with an optimized standard program exhibit the lowest standard deviation and the highest Weibull modulus. In contrast, the standard deviations increase significantly with a 40% higher laser scanning speed and a 25% reduction in laser power. Furthermore, samples measured in the X-Y printing direction show higher standard deviations and lower Weibull moduli compared to those in the Z printing direction, which is attributed to a greater number of small material defects and pores.

While no pile-up or sink-in effects were observed in the steel samples, the pile-up effect occurred during the hardness measurement of the AlMg1Si alloy, independent of the applied force. The pile-up effect leads to an underestimation of the true contact area, resulting in an overestimation of hardness when using the Oliver and Pharr method. To investigate this effect and apply the necessary correction, indentations were performed under an applied load of 300 mN, followed by optical imaging and subsequent analysis. The results indicate that the measured hardness values should be reduced by approximately 7% to compensate for the pile-up effect.

In future works, the indentation test can be optimized by adjusting test parameters such as force, and loading/holding/unloading time. By making these adjustments, smaller microstructural features such as grain boundaries, as well as precipitates and different phases within the material, can be determined through changes in micro- or nano-hardness. This enables the optimization of the 3D printing process and its post-heat treatments. The measurement of nano-hardness with a substantially lower force of a few nanonewtons (nN) will also be highly valuable, especially for analyzing thin films and new coating materials.

References

[1] O. Abdulhameed, A. Al-Ahmari, W. Ameen, S. H. Mian. Additive manufacturing: Challenges, trends, and applications. Advances in Mechanical Engineering, 11(2):1–27, 2019. https://doi.org/10.1177/1687814018822880

[2] D. Bourell, J.P. Kruth, M. Leu, G. Levy, D. Rosen, A.M. Beese, A. Clare. Materials for additive manufacturing. CIRP Annals, 66(2):659–681, 2017. https://doi.org/10.1016/j.cirp.2017.05.009

[3] E. Broitman. Indentation Hardness Measurements at Macro-, Micro-, and Nanoscale: A Critical Overview. Tribology Letters, 65(23), 2017. https://doi.org/10.1007/s11249-016-0805-5

[4] N.E. Gorji, R. O´Conner, D. Brabazon (2020). X-ray Tomography, AFM and Nanoindentation Measurements for Recyclability Analysis of 316L Powders in 3D Printing Process". Procedia Manufacturing, 47:1113–1116, 2020. https://doi.org/10.1016/j.promfg.2020.04.127

[5] P. Filippov, U. Koch. Nanoindentation of Aluminum Single Crystals: Experimental Study on Influencing Factors. Materials, 12(22):3688, 2019. https://doi.org/10.3390/ma12223688

[6] M. ArslanHafeez, M. Usman, M.A. Arshad, M. AdeelUmer. Nanoindentation-Based Micro-Mechanical and Electrochemical Properties of Quench-Hardened, Tempered Low-Carbon Steel. Crystals, 10(6):508, 2020. https://doi.org/10.3390/cryst10060508

[7] V. Bonache, E. Rayón, M.D. Salvador, D. Busquets. Nanoindentation study of WC–12Co hardmetals obtained from nanocrystalline powders: Evaluation of hardness and modulus on individual phases. Materials Science and Engineering, 527(12):2935–2941, 2010. https://doi.org/10.1016/j.msea.2010.01.026

[8] C. Fizanne-Michel, M. Cornen, P. Castany, I. Péron, T. Gloriant. Determination of hardness and elastic modulus inverse pole figures of a polycrystalline commercially pure titanium by coupling nanoindentation and EBSD techniques. Materials Science and Engineering: A, 613:159–162, 2014. https://doi.org/10.1016/j.msea.2014.06.098

[9] H. Attar, S. Ehtemam-Haghighi, D. Kent, I.V. Okulov, H. Wendrock, M. Bönisch, A.S. Volegov, M. Calin, J. Eckert, M.S. Dargusch. Nanoindentation and wear properties of Ti and Ti-TiB composite materials produced by selective laser melting. Materials Science and Engineering, 688:20–26, 2017. https://doi.org/10.1016/j.msea.2017.01.096

[10] T. Peng, F. Junyuan, W. Zhenping, H. Xiaofang, Y. Shu, L. Longsheng, Z. Xichun. Influence of grain orientation on hardness anisotropy and dislocation behavior of AlN ceramic in nanoindentation. Ceramics International, 47(14):20298–20309, 2021. https://doi.org/10.1016/j.ceramint.2021.04.038

[11] S. Ali. Elastic Properties and Hardness of Mixed Alkaline Earth Silicate Oxynitride Glasses. Materials, 15(14):5022–5037, 2022. https://doi.org/10.3390/ma15145022

[12] D. Rogala-Wielgus, B. Majkowska-Marzec, A. Zieliński, M. Bartmański, B. Bartosewicz. Mechanical Behavior of Bi-Layer and Dispersion Coatings

Composed of Several Nanostructures on Ti13Nb13Zr Alloy. Materials, 14(11):2905–2924, 2021. https://doi.org/10.3390/ma14112905
[13] M. Dada, P. Popoola, N. Mathe, S. Adeosun, S. Pityana. Investigating the elastic modulus and hardness properties of a high entropy alloy coating using nanoindentation. International Journal of Lightweight Materials and Manufacture, 4(3):339–345, 2021. https://doi.org/10.1016/j.ijlmm.2021.04.002
[14] F. Khodabakhshi, M.H. Farshidianfar, A.P. Gerlich, A. Khajepour, V. Nagy Trembošová, M. Mohammadi, S.I. Shakil, M. Haghshenas. Nanoindentation plasticity and loading rate sensitivity of laser additive manufactured functionally graded 316L and 410L stainless steels. Materials Science and Engineering: A, 862: 144437, 2023. https://doi.org/10.1016/j.msea.2022.144437
[15] A. Kurdi, T. Tabbakh, A.K. Basak. Microstructural and Nanoindentation Investigation on the Laser Powder Bed Fusion Stainless Steel 316L. Materials, 16(17):5933, 2023. https://doi.org/10.3390/ma16175933
[16] E. Giarmas, E.K. Tzimtzimis, N. Kladovasilakis, D. Tzovaras, D. Tzetzis. Nanoindentation Creep Behavior of Additively Manufactured H13 Steel by Utilizing Selective Laser Melting Technology. Materials, 17(15):3756, 2024. https://doi.org/10.3390/ma17153756
[17] A. Kurdi, A. Aldoshan, F. Alshabouna, A. Alodadi, A. Degnah, H. Alnaser, T. Tabbakh, A.K. Basak. Investigation into the Microstructure and Hardness of Additively Manufactured (3D-Printed) Inconel 718 Alloy. Materials, 16(6):2383, 2023. https://doi.org/10.3390/ma16062383
[18] N. Kladovasilakis, P. Charalampous, K. Tsongas, I. Kostavelis, D. Tzovaras, D. Tzetzis. Influence of Selective Laser Melting Additive Manufacturing Parameters in Inconel 718 Superalloy. Materials, 15(4):1362, 2022. https://doi.org/10.3390/ma15041362
[19] F. Dababneh, H. Taheri. Investigation of the influence of process interruption on mechanical properties of metal additive manufacturing parts. CIRP Journal of Manufacturing Science and Technology, 38:706–716, 2022. https://doi.org/10.1016/j.cirpj.2022.06.008
[20] C. Schneider-Maunoury, A. Albayda, O. Bartier, L. Weiss, G. Mauvoisin, X. Hernot, P. Laheurte. On the use of instrumented indentation to characterize the mechanical properties of functionally graded binary alloys manufactured by additive manufacturing. Materials Today Communications, 25:101451, 2020. https://doi.org/10.1016/j.mtcomm.2020.101451
[21] German Industrial Standard DIN EN ISO 14577-1:2015-1, Metallische Werkstoffe - Instrumentierte Eindringprüfung zur Bestimmung der Härte und anderer Werkstoffparameter- Teil_1: Prüfverfahren (ISO_14577-1:2015). Deutsche Fassung EN_ISO_14577-1:2015, Berlin.
[22] A. C. Fischer-Cripps. Nanoindentation (Mechanical Engineering Series). Springer, New York, 2011. ISBN: 978-1-4419-9871-2. https://doi.org/10.1007/978-1-4419-9872-9
[23] A. Steinacker. Produkt-Training Instrumentierte Eindringprüfung: Theoretische Grundlagen. Company prospect 2019.
[24] G.M. Pharr, W.C. Oliver, F.R. Brotzen. On the generality of the relationship among contact stiffness, contact area, and elastic modulus during indentation.

Journal of Materials Research, 7(3): 613–617, 1992. https://doi.org/10.1557/JMR.1992.0613
[25] M. Göken. Nanoindentation Testing. in: H. Biermann and L. Krüger (Eds.). Modern Methods of Materials Testing. p. 299-347. WILEY-VCH, Weinheim, 2015. ISBN: 978-3-527-33413-1.
[26] D.R. Tadjiev, R.J. Hand, S.A. Hayes. Calibrating a nanoindenter for very shallow depth indentation using equivalent contact radius. Philosophical Magazine A, 90(13): 1819–1832, 2010. https://doi.org/10.1080/14786430903571420
[27] W. Li, N. Bian, K.M. Nagaraja, X. Zhang, H. Lu. Exploratory Studies of Mechanical Properties, Residual Stress, and Grain Evolution at the Local Regions near Pores in Additively Manufactured Metals. Materials, 17(13): 3277, 2024, https://doi.org/10.3390/ma17133277
[28] D. Jafari, K.J.H. van Alphen, B.J. Geurts, W.W. Wits, L.C. Gonzalez, T.H.J. Vaneker, N.U. Rahman, G.W. Römer, I. Gibson. Porous materials additively manufactured at low energy: Single-layer manufacturing and characterization. Materials & Design, 191: 108654, 2020. https://doi.org/10.1016/j.matdes.2020.108654
[29] K.W. McElhaney, J.J. Vlassak, W.D. Nix. Determination of indenter tip geometry and indentation contact area for depth-sensing indentation experiments. Journal of materials research, 13(5):1300–1306, 1998. https://doi.org/10.1557/JMR.1998.0185
[30] N. Moharrami, S.J. Bull. A comparison of nanoindentation pile-up in bulk materials and thin films. Thin Solid Films, 572:189–199, 2014. https://doi.org/10.1016/j.tsf.2014.06.060
[31] J.B. Quinn, G.D. Quinn. A practical and systematic review of Weibull statistics for reporting strengths of dental materials. Dent Material, 26(2):135–47, 2010. https://doi.org/10.1016/j.dental.2009.09.006
[32] Brevier TECHNISCHE KERAMIK. Eigenschaften technischer Keramik. https://www.keramverband.de/brevier_dt/5/3/3/5_3_3_4.htm (assessed on 01.10.2024)
[33] V. Sinka, M. Selecka, A . Šalak. Influence of iron powder grade and manganese carrier on the homogeneity modulus of sintered Mn steels. Materials Science Forum 416–418:455–463, 2003. https://doi.org/10.4028/www.scientific.net/msf.416-418.455
[34] B.C. Choi, C.Y. Kang, K.W. Nam. Characteristics for Weibull Distribution of Vickers Hardness to Different Cold Rolled STS316L. Journal of Power System Engineering 23(2):85–90, 2019. https://doi.org/10.9726/kspse.2019.23.2.085
[35] N. Biery, M. De Graef, J. Beuth, R. Raban, A. Elliott, T.M. Pollock, C. Austin. Use of weibull statistics to quantify property variability in TiAl alloys. Metall Mater Trans, A 33:3127–3136, 2002. https://doi.org/10.1007/s11661-002-0298-8
[36] Ç. Yüksel. Weibull analysis of fluidity and hardness of ultrasonically degassed secondary Al7Si0.3Mg aluminum alloy. China foundry, 16(5): 352–357, 2019. https://doi.org/10.1007/s41230-019-9029-2
[37] H.J. Neilson, A.S. Petersen, A.M. Cheung, S.J. Poon, G.J. Shiflet, M.Widom, J.J. Lewandowski. Weibull modulus of hardness, bend strength, and tensile strength of

Ni−Ta−Co−X metallic glass ribbons. Materials Science and Engineering: A 634: 176–182, 2015. https://doi.org/10.1016/j.msea.2015.03.006
[38] R.B. Abernethy. The New Weibull Handbook. 5th edition, North Palm Beach, Fl., 2006, p. 4
[39] Khan Academy. Ausreißer mit Hilfe der 1,5*IQR-Regel bestimmen. https://de.khanacademy.org/math/statistics-probability/summarizing-quantitative-data/box-whisker-plots/a/identifying-outliers-iqr-rule (assessed on 10.10.2024)
[40] MathWorks. KStest-One-sample Kolmogorov-Smirnov test. https://de.mathworks.com/help/stats/kstest.html (assessed on 14.05.2025)

Gia Khanh Pham, Ruth Domes, Ümit Mavis, Johannes Ernstberger, Christian Seidel, Constanze Eulenkamp, Christine Hausner-Henzel
Department of Applied Sciences and Mechatronics
Munich University of Applied Sciences, Munich, Germany

Anh Son Nguyen
School of Materials Science and Engineering, Hanoi University of Science and Technology, Hanoi, Vietnam

Gia Vu Pham
Institute for Tropical Technology, Vietnam Academy of Science and Technology, Hanoi, Vietnam